JOURNAL OF SPACECRAFT AND ROCKETS
Vol. 35, No. 6, November–December 1998

Effects of Mach Number on Supersonic Wraparound Fin Aerodynamics

Thomas C. McIntyre*
U.S. Air Force Institute of Technology, Wright–Patterson Air Force Base, Ohio 45433-7765
Rodney D. W. Bowersox†
University of Alabama, Tuscaloosa, Alabama 35487-0280
and
Larry P. Goss‡
Innovative Scientific Solutions, Inc., Dayton, Ohio 45440-3638

An experimental Mach number parametric ($M \in [2.15, 3.83]$) study was conducted to investigate the apparent rolling-moment reduction with increasing Mach number noted in flight-test experiments. The aerodynamic loading and the surface flow in the fin region of wraparound fin missiles in high-Reynolds-number ($Re_C \in 0.3 \times 10^6$ to 0.9×10^6) supersonic cross streams were investigated using photoluminescent pressure-sensitive paint and surface oil-flow visualizations with fluorescent pigment as the seeding medium. Schlieren photography was used to characterize the fin-generated shock structures. Two curved-fin missiles were tested, one having a solid fin and the other a slotted fin. The fin pressures were integrated for rolling moments; these data confirm the solid-fin missile reduction in rolling moment with increasing Mach number. The slotted-fin missile exhibited a similar rolling-moment Mach number dependence. Analysis of the pressure distributions, surface streamlines, and shock structures indicated that the flowfields experienced very strong and complicated inviscid–viscous interactions and that these interactions had a significant impact on the aerodynamic loading of the fins. Finally, the slotted-fin missile demonstrated the potential for increased roll stability and reduced wave drag.

Nomenclature

A = missile cross-sectional area, mm^2
C_L = $L/(q_\infty Ad)$
d = missile diameter, mm
I_0/I = pixel luminescence ratio (I_0 = ambient reference intensity)
K_q = Stern–Volmer constant
L = rolling-moment, N-m
P_{O_2} = partial pressure of oxygen
p = static pressure, atm
$p_{t\infty}$ = freestream total pressure, atm
q_∞ = freestream dynamic pressure, atm
Re_C = Reynolds number based on fin chord length

Introduction

WRAPAROUND fins (WAFs; Fig. 1) have been used on tube-launched missiles and dispenser-launched projectiles. Modern advances in stealth technology have made the use of missiles equipped with WAFs desirable because they can be stowed to reduce the radar cross section of the aircraft. Recent studies have identified several roll- and pitch-moment instabilities.[1] The roll reversal at transonic conditions is the most recognized instability. The rolling moment of the WAF is positive at subsonic velocities (defined here to mean that the missile rolls toward the concave side of the fin). A roll reversal occurs at Mach 1.0. Range tests[1–4] have indicated that the magnitude of the rolling moment decreases with increasing Mach number and that a second rolling-moment reversal may occur at high supersonic speeds ($M \sim 4.5$–4.7). Abate[5] postulated that the loss of static stability at high supersonic Mach numbers is related to the complex shock structure in the fin region.

Tilmann et al.[6] and Tilmann and Bowersox[7] examined experimentally and numerically the flow structure in the vicinity of a single fin mounted onto a blended cylindrical-body wind-tunnel wall model at Mach 3.0 and 5.0. Those studies indicated that the flowfield was highly asymmetric about the WAF, with a stronger bow-shock structure on the concave side of the fin. The viscous computational fluid dynamics (CFD) solutions indicated that, on the concave side of the fin, the shock is focused, creating a very high-pressure region between the fin and its center of curvature, which resulted in relatively high surface pressures near the midspan of the fin. In contrast, on the convex side of the fin, surface pressure is relatively independent of location along the span. In addition to the shock-structure asymmetries, a juncture vortex on the concave side of the fin was identified. This viscous structure also was found to influence asymmetrically the pressure loading of the curved fin. The numerical viscous solutions did predict a reduction in rolling moment at Mach 5.0 as compared to Mach 3.0. However, a roll reversal was not observed.

The primary purpose of the present study is to examine experimentally the Mach number dependence of the aerodynamic loading and viscous surface flow in the fin region of the WAF projectiles. Two full axisymmetric four-fin missile models were tested. One model was equipped with solid fins, and the other had slotted fins. The purpose of the slot was to provide pressure relief, thereby reducing the Mach number dependence of the rolling moment. Pressure-sensitive paint (PSP), surface oil-flow visualizations, and schlieren photography were used to analyze the fin pressure loading, viscous streamline structure, and shock structure, respectively. A high-Reynolds-number Mach number parametric study was performed, where the Mach number was varied over the range 2.15–3.83. In addition to the Mach number parametric investigation, the single-fin configuration from Refs. 6 and 7 was examined using the same PSP apparatus. A comparison of the experimental results to the CFD predictions of Refs. 6 and 7 was performed.

Experimental Facilities

The two four-fin models used for testing are shown in Figs. 1 and 2 (side and rear views). The projectile diameter was used to

Received March 27, 1998; revision received May 26, 1998; accepted for publication May 27, 1998.

*Graduate Research Assistant; 2nd Lieutenant; currently Project Officer, Launch Programs, Space and Missile Systems Center, Medium Launch Vehicle Office (Delta II). Member AIAA.

†Assistant Professor, Department of Aerospace Engineering and Mechanics. Senior Member AIAA.

‡Research Scientist and President, 2786 Indian Ripple Road. Senior Member AIAA.

Table 1 Nominal test conditions

Mach no.	$p_{t\infty}$, atm	Re_C, $\times 10^6$	L, N-m Solid fin	L, N-m Slotted fin
2.15	2.8	0.33	−0.046	−0.052
2.15	6.1	0.72	−0.048	−0.050
2.15	7.0	0.83	−0.052	−0.042
2.41	3.9	0.40	−0.032	−0.057
2.41	7.1	0.74	−0.036	−0.047
2.41	8.6	0.90	−0.041	−0.073
2.86[a]	2.1	0.37	——	——
2.86	5.8	0.48	−0.031	−0.062
2.86	8.2	0.68	−0.028	−0.020
2.86	9.8	0.81	−0.032	−0.052
3.25	8.9	0.60	−0.016	−0.041
3.25	10.4	0.70	−0.032	−0.055
3.50	8.7	0.52	−0.017	−0.061
3.50	10.0	0.60	−0.024	−0.039
3.50	11.3	0.68	−0.025	−0.055
3.83	11.5	0.58	−0.022	——
3.83	12.1	0.61	−0.016	——

[a]Single-fin experiments.

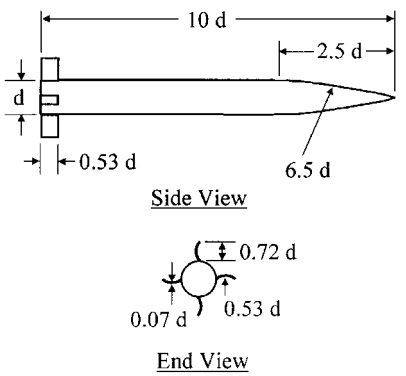

Fig. 1 Schematic of solid-fin model (not drawn to scale).

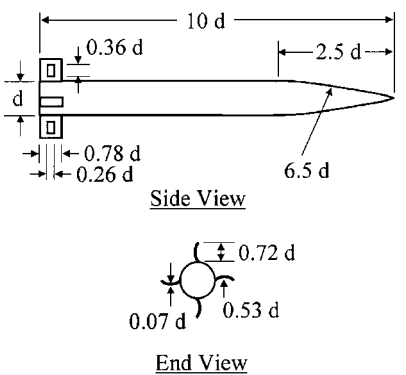

Fig. 2 Schematic of slotted-fin model (not drawn to scale).

scale the major physical features of the models. Both models had a diameter of 1.91 cm. The slotted-fin model had 28.6% more surface area than the solid-fin model, when viewed from the side.

A variable-Mach supersonic blowdown wind tunnel located at Wright–Patterson Air Force Base was used for testing the missile models shown in Figs. 1 and 2. The wind tunnel provided a uniform Mach number distribution across the test section to within 2.0%. The test-section static pressure, total pressure, and total temperature were recorded during each run. The total temperature was 295 K for all runs. The expected uncertainties are described in the Uncertainty Analysis section. The nominal flow conditions for each test condition are summarized in Table 1. The test-section dimension of this tunnel (15.24 × 15.24 cm) limited the lowest Mach number to 2.15. For Mach numbers lower than this, the missile nose shock reflections off the tunnel walls intersected with the tail of the missile.

PSP tests also were conducted on the single-fin model described in Refs. 6 and 7. A schematic of this model is presented in Fig. 3.

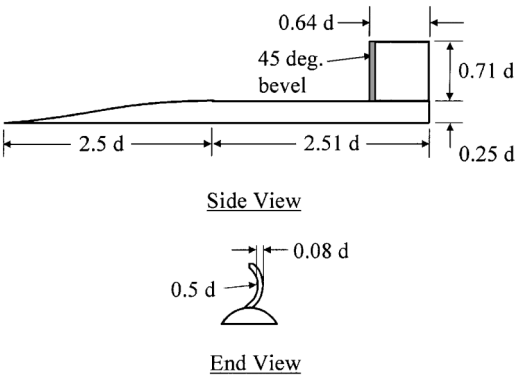

Fig. 3 Schematic of single-fin model (not drawn to scale).

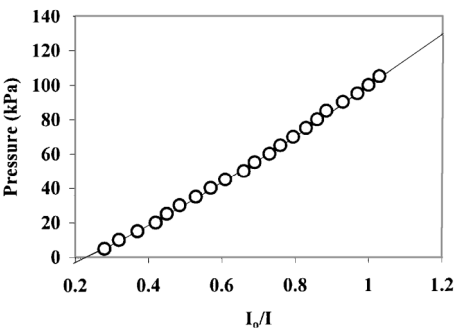

Fig. 4 PtOEP pressure calibration.

The Mach 3 pressure-vacuum wind tunnel described in Ref. 6 was used for the single-fin model testing.

Experimental Techniques

PSP

PSP was used to analyze fin pressures. This nonintrusive method provided continuous pressure data on the missile body and fins. Because the fins are the source of rolling moment due to pressure forces, the pressure measurements were concentrated in the fin region.

PSP technology has been documented extensively.[8–10] Measurements are based on the phenomenon of photoluminescence. A probe molecule absorbs a photon of specific energy, exciting it to a higher state. The molecule then returns to the ground state by emitting a photon of lower energy. However, if an oxygen molecule is present, the excess energy of the probe molecule will be transmitted to the oxygen during a collisional deactivation. The oxygen-quenching phenomenon can be modeled with the Stern–Volmer relationship:

$$I_0/I = 1 + K_q P_{O_2} \tag{1}$$

Variations in temperature affect I_0 and K_q, causing temperature sensitivities. In the present study, short test times (<30 s) and 30-min reservoir recharge periods resulted in the missile surface remaining at room temperature (295 K).

The Stern–Volmer equation was applied by taking images at a reference pressure condition (ambient pressure) and at the test condition. The ambient pressure intensity I_0 then was divided by the test intensity I. The ratio of intensities was calibrated at room temperature. The calibration curve obtained is shown in Fig. 4. The correlation coefficient for the curve fit was 0.999.

The pressure-sensitive material applied to the WAF missiles was developed at the Arnold Engineering Development Center (AEDC).[11] The probe molecule consisted of platinum octaethylporphyrin (PtOEP) diluted in toluene and sprayed over a white Krylon titanium dioxide primer layer of paint. This primer removed intensity variations in the metallic construction of the missile fins and body. The maximum excitation wavelengths of the PtOEP paint are at 380 and 540 nm, with emissions at 650 nm. A scientific-grade Pixel Vision charge-coupled device (CCD) camera recorded photographs, using a 516 × 516 pixel monochrome CCD and 50-mm lens.

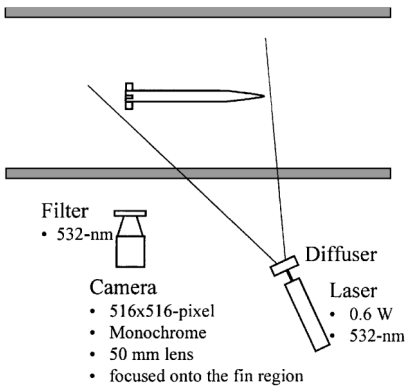

Fig. 5 Top-view schematic of the PSP experimental setup.

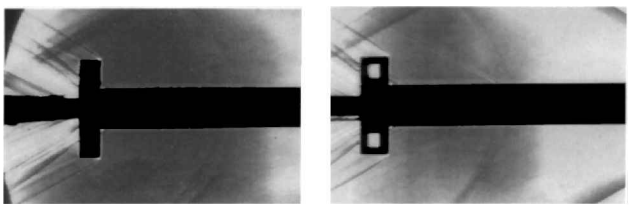

a) Mach 2.15

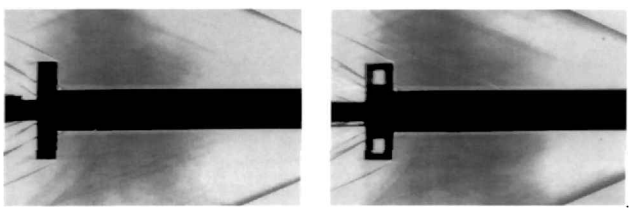

b) Mach 2.88

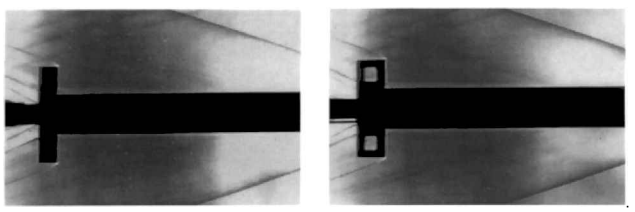

c) Mach 3.83

Fig. 6 Solid- and slotted-fin schlieren images (vertical knife edge).

The paint was excited with a Spectra-Physics Millennia continuous-wave laser at 532 nm. The 0.6-W laser light was diffused by a plate of packed ground glass and shined on the test subject. A red filter was placed over the camera lens to ensure that only paint emissions would be captured on the CCD. Figure 5 is a schematic of the setup. Ten air-off images were taken and averaged to remove systematic ambient nonuniformities.

Surface Oil-Flow and Schlieren Photography

To obtain surface streamlines, a fluorescent powdered yellow dye was diluted into 200 cS of silicon oil. During the tunnel run, the dye was illuminated with two 115-V Black-Ray B-100A ultraviolet lamps. Schlieren photography, with a continuous mercury-vapor light source, was used to characterize the shock structures. A vertical knife-edge arrangement was used to improve the definition of the shock/boundary-layer interactions. For both the surface oil flow and the schlieren photography, images were acquired with a Kodak DCS 420 color digital camera (ISO setting of 200 and shutter speed of 1/30th s).

Experimental Results

Schlieren Imaging

Presented in Fig. 6 are representative schlieren photographs for the solid- and slotted-fin missiles for Mach numbers 2.15, 2.88, and 3.83. These images highlight the complex nature of the present flowfield near the fin regions of the missiles. Important details are revealed about shock locations. A slightly detached bow shock is visible just upstream of the fin. When this shock interacted with the fuselage boundary layer, a lambda shock was formed, which appeared just upstream of the base of the fin leading edge. Also noticeable in the schlieren images are oblique shock-wave structures exiting the fin region. The angle and vertical extent up the fin decreased with decreasing Mach number. These shock waves were produced by viscous phenomena near the fin–fuselage juncture—a vortex on the convex side and a flow separation on the concave side (these features are discussed in detail in the next section).

Surface Oil-Flow Visualizations

As mentioned in the Introduction, one of the purposes of the study was to examine the effects of Mach number on the surface flow. To that end, Fig. 7 shows the surface oil-flow visualization results for the solid- and slotted-fin missiles for $M = 2.15$, 2.88, and 3.83. The convex fin is on the top and the concave fin is on the bottom. Qualitatively, the fin surface streaklines are very similar to those of the single-fin numerical solutions of Tilmann et al.[6]

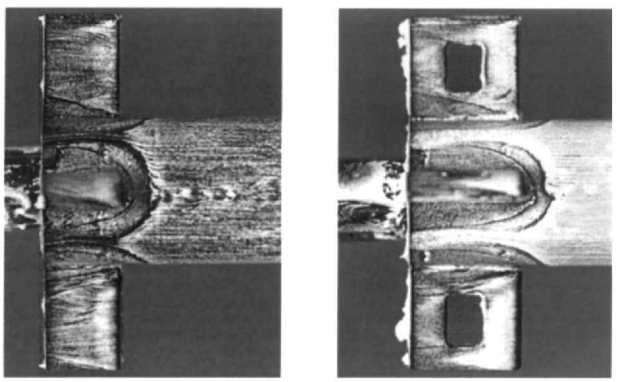

a) Mach 2.15

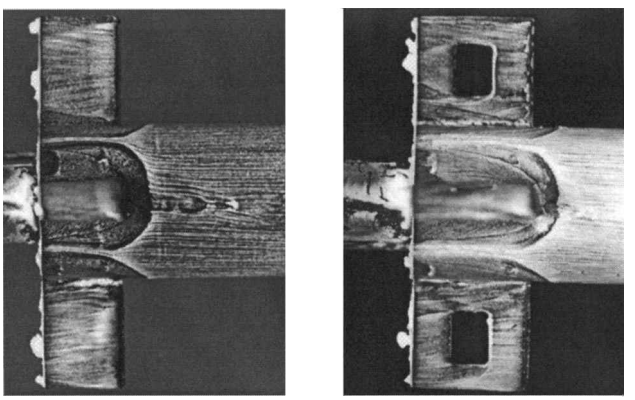

b) Mach 2.88

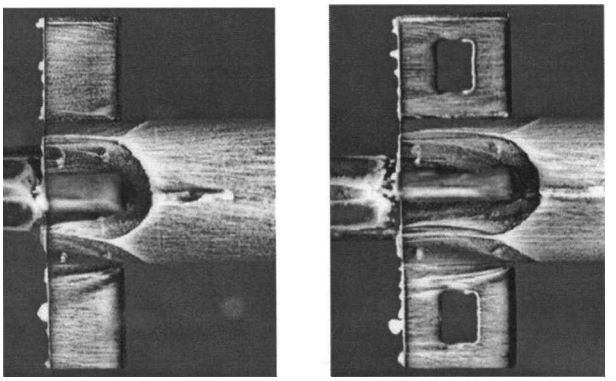

c) Mach 3.83

Fig. 7 Solid- and slotted-fin surface oil-flow visualizations.

However, the missile body streamlines did not compare well because the multiple fins in the present configuration created shock-induced compressions in the oil flow between the two fins. Examination of these images reveals the Mach number dependence on the salient flowfield features described in detail in Ref. 6.

Concentrating first on the surface phenomena on the concave side of the solid fin (bottom fin in Fig. 7), the flow near the fin root was characterized by a vortex embedded in the juncture of the fin and fuselage. The relatively large accumulation of oil that began near the fin leading-edge root region and progressed downstream at an angle relative to the fuselage provided an indication of the size and shape of the vortex. The size of the dark regions above and below the vortex, which indicate streamline divergence toward the vortex, also provided an indication of the vortex strength, i.e., the strength of the entrainment process. At Mach 2.15, the secondary flow motion influenced a relatively large (compared to the higher Mach numbers) portion of the fin. At Mach 3.83, the vortex was confined to a very small region. However, the strength of the vortex appears to have increased with increasing Mach number, where a large portion of the flow, as indicated by the strong divergence of streaklines (dark region just outward of the juncture vortex) over the fin has been entrained into the vortex. Tilmann et al.[6] have suggested that this viscous phenomenon may, in part, be responsible for the reduced rolling moment at the high Mach numbers.

The surface oil-flow visualizations also highlight the flow pattern near the outer tip of the fin. The dark wedge-structure oil pattern, which emanated from the leading-edge tip region, provided evidence for a slight leakage or separation from the fin, which, like the juncture vortex, was more prominent at the low Mach number. For the higher-Mach-number experiments ($\geq$2.41), the flow over the main region of the fin, away from the juncture–vortex and the tip, was relatively orderly. For the Mach 2.15 case, a large disturbance is noticeable emanating from the leading-edge root and proceeding to the trailing-edge midfin height. It is thought that this feature created a region of relatively low pressure and thus had a strong impact on the rolling moment.

On the concave side of the fin (top fin in Fig. 7), the juncture region was characterized by a separation, indicated by the wedge-like region near the root that is void of oil. As the Mach number was increased, the size of the separation region decreased dramatically. The oil patterns near the tip suggest that the flow diverged slightly out toward the fin bevel. As on the convex side, the flow over a large region of the fin (away from the root separation) was reasonably well ordered, with a slight divergence near the aft region of the fin.

The surface oil-flow visualizations in Fig. 7 also highlight the fuselage flow. Progressing in the flow direction, i.e., from right to left, the asymmetric lambda-shock separation line is the first surface disturbance. As expected, as the Mach number was increased, the shock structure became more oblique. The lambda shock was slightly more normal on the convex side and slightly more oblique on the concave side of the fin. The next line of separation indicates the location of the fin–fuselage horseshoe-vortex system. Like the shock structure, the horseshoe vortex was also asymmetric around the fin. As the Mach number was increased from 2.15 to 3.83, the horseshoe vortex moved closer to the fin on the concave side. However, on the convex side of the fin, the horseshoe-vortex position remained fixed as the Mach number was varied.

The slotted-fin surface oil-flow visualizations indicate that the presence of the slot dramatically changed the surface flowfield. Concentrating on the convex side of the fin (bottom fin in Fig. 7) at Mach 2.15, the juncture vortex described earlier was present upstream of the slot. However, the vortex intersected the slot region of the fin, and the strength of the vortex was reduced aft of the slot. This slot interaction effect was observed to diminish with increasing Mach number; this occurred because the vortex region became more confined to the fuselage as the Mach number was increased. Furthermore, the slot appears to have eliminated the tip leakage separation near the fin tips.

The slots also had a significant impact on the fuselage flow patterns. First, at $M = 2.15$, the extent around the fin of the lambda shock was greatly reduced, which indicated that the pressure relief

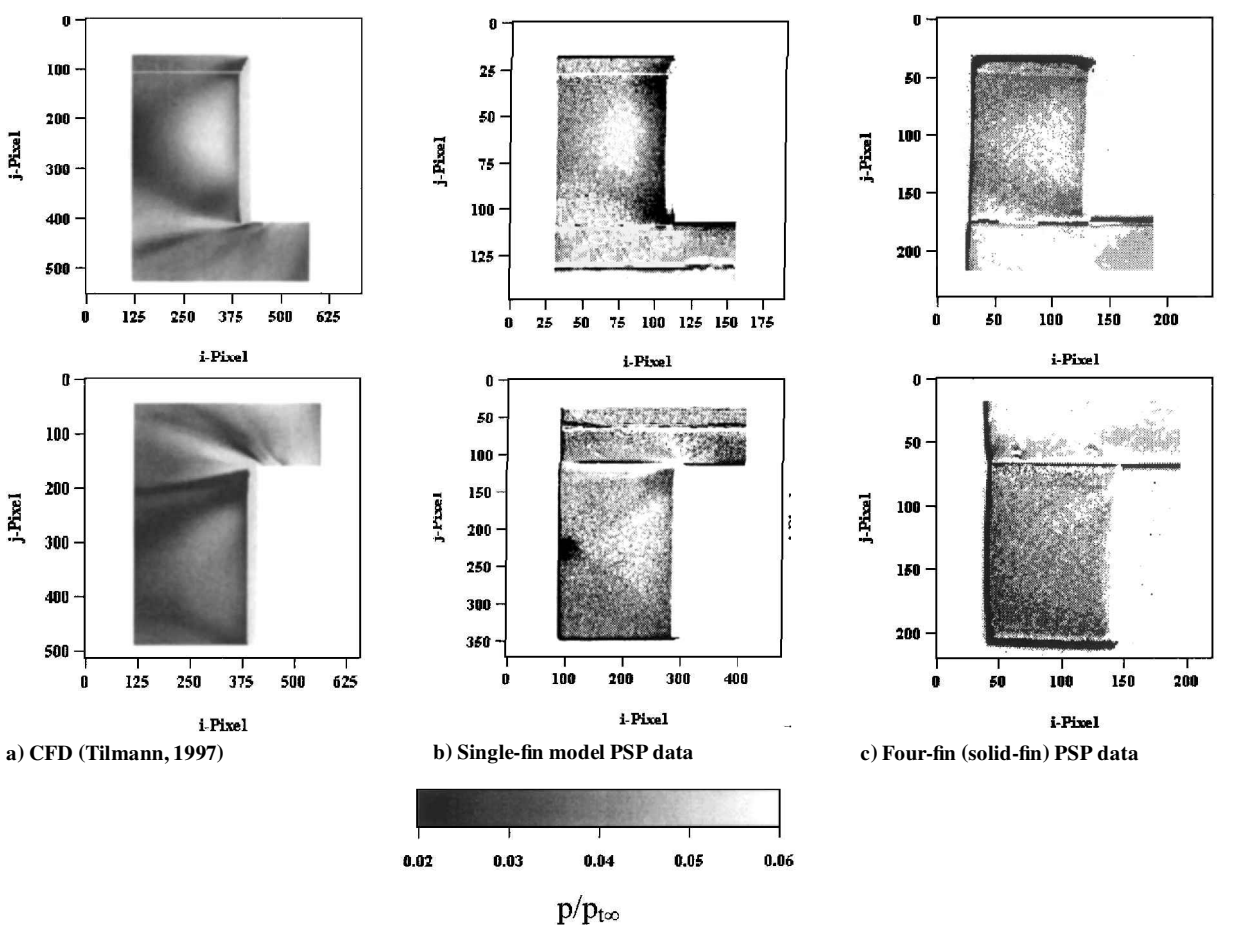

Fig. 8 Comparison of pressure fields at Mach 2.9 (convex side of fin on the top, and concave side of fin on the bottom).

provided by the slot reduced the apparent blockage of the fin. This pressure relief translates into potential wave drag reduction; this effect was so strong that a relatively large region of undisturbed flow existed between the shock structures generated by adjacent fins. This region of undisturbed flow was not present for any of the solid-fin experiments. Interestingly, as the Mach number was increased past 2.88, the shock structure upstream of the fin became more symmetrical and somewhat independent of Mach number. As the Mach number was increased, the adjacent fin-generated shock structure interactions became more severe and the undisturbed region diminished in size. On the concave side of the fin, at Mach 3.83, the undisturbed region was no longer present, and the shocks appear to have interacted with the horseshoe vortex, creating a complex flow region.

PSP

PSP was applied to the wall-mounted, single-fin model of Ref. 6 and the four-fin models (Figs. 1 and 2) for validation and flowfield analysis purposes, respectively. Figure 8 compares viscous CFD results[6] for the single-fin configuration to present PSP measurements for both the single-fin and four-fin models. A reasonable degree of dynamic similarity existed among the CFD calculations, the single-fin model, and the axisymmetric four-fin model, where the Mach numbers were matched to within the measurement uncertainty and the Reynolds numbers based on fin chord were reasonably consistent. The flow conditions and fin geometry for the single-fin CFD calculations[6] were chosen to match the single-fin experimental test case ($M = 2.88$ and $Re_C = 3.7 \times 10^5$). For the four-fin model, the Mach number was set to 2.88 and the Reynolds number for the data shown in Fig. 8 was somewhat higher at 4.8×10^5. As the data in Fig. 8 indicate, good qualitative and quantitative agreement was observed between the single- and four-fin models and the CFD solution. The black spot in the aft, middle portion of the convex fin (Fig. 8b) resulted from an accumulation of Krylon primer, which flawed the data in this location.

The solid-fin images in Fig. 8 show high pressures along the leading edge of the fin. These strong stagnation pressures were expected for the relatively blunt fins in this study. On the concave side fin surface, the compressive effects of fin curvature[6] created a triangular region of high pressure. Preceding this region was a small lip of low pressure caused by the expansion that followed the detached shock in front of the fin. The bottom portion of the concave fin showed another pressure increase, resulting from boundary-layer compression that occurred between fins. The wedge-shaped region of high pressure in the juncture depicts the influence of the fin–body juncture vortex[6] on the pressure field. This vortex was created at the leading edge of the fin–body juncture and increased in size and strength as the flow proceeded downstream.

Figure 9 shows a representative PSP image for the solid- and slotted-fin at $M = 2.15$. In these images, the convex side of the fin is shown at the bottom of the missile, the concave side on the top, and a top view in the middle. As indicated in Fig. 9, the pressure distributions on the fin and fuselage in the vicinity of the fin were strongly dependent on the viscous phenomena, as described in the Surface Oil-Flow Visualization section. The detached shock formed in front of the fins is also clearly visible in the PSP images.

The slotted-fin images in Fig. 9 display many of the features of the solid fin. On the fin, the slot appears to have little effect on the pressure distribution, except for the slot walls themselves. The same triangular region of high pressure, which was interrupted by the slot, was also present on the concave side surface of the fin. The juncture vortex appeared to have been undisturbed upstream of the slot but disappeared downstream of the slot. It is likely that momentum flux through the slot from the concave side of the fin dispersed the vortex structure.

Rolling Moments

The PSP images at each Mach number were processed for rolling moments. The magnitudes of the rolling moments are shown in Fig. 10. To avoid cooling effects on the PtOEP paint, the first three photographs at each flow condition were used. During this 12-s period, the total pressure varied, resulting in the Reynolds number

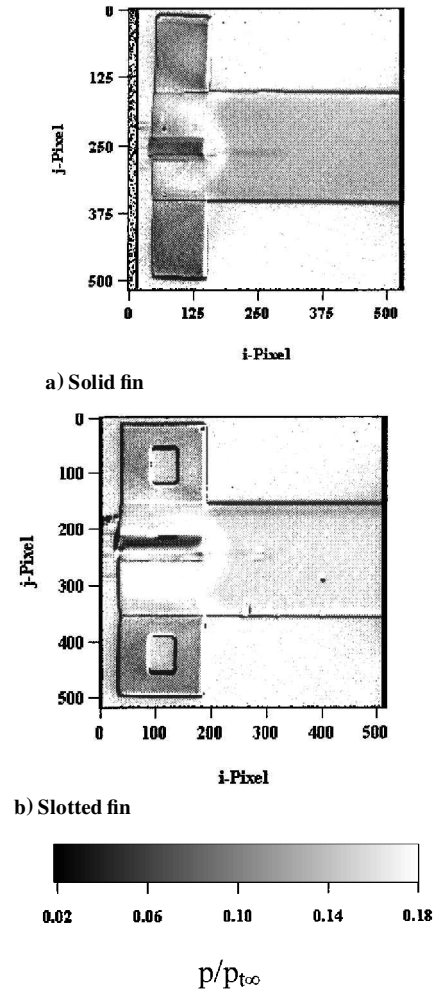

Fig. 9 Comparison of solid- and slotted-fin pressure distributions at $M = 2.15$.

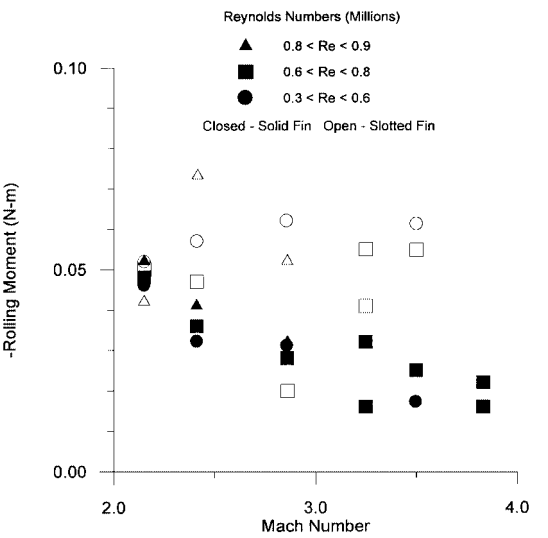

Fig. 10 Rolling moments.

variations in Table 1. The rolling moments at each flow condition for both models also are shown in Table 1.

The Reynolds number has been shown to have a strong impact on the rolling-moment coefficient, as evident from data obtained at AEDC, NASA Langley Research Center, and NASA's Jet Propulsion Laboratory.[7] To minimize the Reynolds number influences, the data plotted in Fig. 10 were separated into the three Reynolds number ranges as annotated. As indicated, the Reynolds number variations did produce increased scatter of the data. However, all

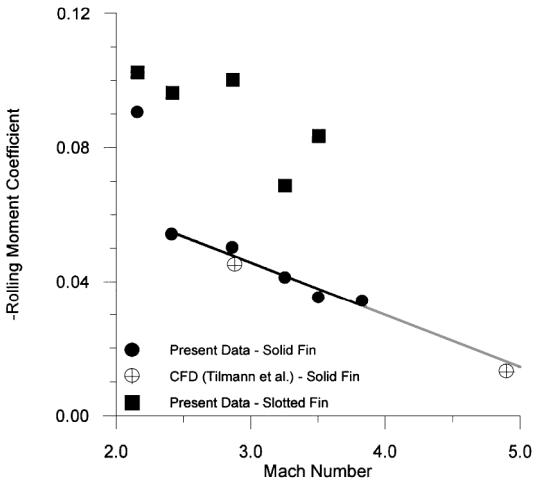

Fig. 11 Rolling-moment coefficients.

of the data suggest a strong reduction in the rolling moment with increased Mach number. This result confirms the test-range trend described by Abate.[5]

The slotted-fin rolling moments also are plotted in Fig. 10. The rolling-moment scatter of the slotted fin was higher because of the increased uncertainty associated with locating the slot in the data reduction procedure. This effect, coupled with the aforementioned Reynolds number variations, obscured the Mach number trends. This shortcoming is discussed in the remainder of this section.

The rolling-moment coefficients are plotted in Fig. 11. To reduce the apparent experimental scatter, the data shown in Fig. 11 correspond to a Reynolds number of nominally 0.6×10^6 ($\pm 10\%$) and a dynamic pressure of 100 kPa ($\pm 10\%$). However, for the Mach 2.15 and 2.41 cases, the plotted data correspond to Reynolds numbers of 0.33 and 0.40, respectively. For the Mach numbers with more than one data point within the 10% range, those values were averaged into the single points plotted in Fig. 11. The expected uncertainties are described in the Uncertainty Analysis section. Also shown in Fig. 11, for comparison purposes, are the rolling-moment CFD predictions (the dynamic pressures were 40 and 99 kPa at $M = 2.9$ and 4.9, respectively) of Tilmann et al.[6] Considering the relatively large uncertainty associated with the experimental data (see the next section) and the slightly different fin models, the agreement between the CFD predictions and experimental data is considered to be rather fortuitous. The solid-fin data confirmed the previously observed rolling-moment coefficient reduction with increasing Mach number. The dark line indicates a linear curve fit for $M \in [2.41, 3.83]$, and the light line is an extrapolation to Mach 5. As indicated, the CFD predictions followed this extrapolation. The Mach 2.15 data point did not follow this trend. The large flow disturbance across the fin described in the Oil-Flow Visualization section is likely the cause of this discrepancy. Limited PSP experiments also were performed at Mach 2.28, and the corresponding rolling moment was well above the linear trend (similar in magnitude to the $M = 2.15$ data). If the linear trend were to persist to higher Mach numbers, then the rolling moment would reach zero at $M = 5.9$.

The slotted-fin rolling-moment coefficients calculated as described in the preceding paragraph also are given in Fig. 11. In general, the rolling-moment coefficients were roughly twice those of the solid fin, and, as discussed earlier, the scatter in the data was larger. However, these data also suggest a decrease in the rolling-moment coefficient with increasing Mach number.

Uncertainty Analysis

Taking into account transducer uncertainties, the freestream flow-condition uncertainties were estimated as $\pm 0.3\%$, 2.5%, and 2.0% for the Mach number, dynamic pressure, and Reynolds number, respectively. The calibration curve used for PSP measurements resulted in an uncertainty of ± 2.068 kPa, which, coupled with the transducer calibration uncertainties, produced $p/p_{t\infty}$ uncertainties of ± 0.009. The normalization procedure was used to minimize the uncertainties introduced by the light source and camera; hence those errors were neglected. Also, because the model temperature did not deviate substantially from room temperature, the surface-temperature-induced effects also were assumed to be negligible. The pressure data were used to determine rolling moments, which, coupled with the pixel resolution, resulted in a rolling-moment uncertainty of ± 0.0053 N-m for the solid fin and ± 0.0064 N-m for the slotted fin. This error contribution, along with wind-tunnel errors, resulted in an average rolling-moment coefficient error of ± 0.0066 for the solid fin and ± 0.0077 for the slotted fin.

In addition to the inherent random uncertainties of the measurement techniques, two other sources of bias error influenced the rolling-moment data. First, the leading-edge data of the missile fins were neglected in the rolling-moment calculations. These high stagnation pressures were outside the calibration range of the PtOEP paint. Thus, only pressure data on the sides and tips were used to compute a rolling moment. To quantify the error involved in this negligence, the CFD pressure images from Ref. 6 were processed with the same software used for the experimental data. It was found that neglecting the leading-edge contributions to the rolling moment resulted in an underprediction of the rolling-moment coefficient by nominally 2%. Second, the effects of shear stress on the rolling moment also were neglected. The CFD pressure images were again processed using the entire fin. Comparison to the CFD rolling-moment calculations that included the rolling moments indicated that neglecting the shear-stress forces resulted in rolling-moment coefficients that were overestimated by nominally 5%.

Conclusions

The complex viscous flowfield features in the vicinity of the fin for two WAF missiles are characterized as a function of Mach number ($M \in [2.15, 3.83]$) using PSP, surface oil-flow visualizations, and schlieren photography. A complete flowfield description is provided. In summary, the Mach number is found to have a profound impact on both the viscous phenomena and fin loading. The rolling moment decreases rapidly (almost discontinuously) by a factor of nearly 2 between the Mach numbers of 2.15 and 2.41. For Mach numbers of 2.41 and above, the rolling moment decreases almost linearly with increasing Mach number. This trend confirms observed flight-test anomalies.

Adding a slot to the fin for pressure relief was found to dramatically reduce the strength of the shock structure produced by the fin at low Mach numbers. This finding could translate into reduced wave drag. In addition, the rolling-moment magnitudes for the slotted fin, which had a 28.6% larger wetted surface area, were nearly double those of the solid fin. However, a decreasing rolling-moment trend with Mach number also was noticed for the slotted fin.

Acknowledgments

The authors acknowledge Gregg Abate, U.S. Air Force Research Laboratory, Armament Directorate, for providing funding for this project under U.S. Air Force Contract F33610-90-C-2507. The authors also thank Carl Tilmann for providing the computational fluid dynamics data. Alan Forlines, Ben Sarka, Kelly Navarra, and Gary Dale are acknowledged for providing suggestions in support of this research. Finally, the efforts of Andy Pitts, Dave Driscoll (deceased), and Mike Suggs also are gratefully acknowledged.

References

[1] Abate, G. L., and Winchenbach, G. L., "Aerodynamics of Missiles with Slotted Fin Configurations," AIAA Paper 91-0676, Jan. 1991.

[2] Abate, G. L., and Winchenbach, G., "Analysis of Wrap-Around Fin and Alternative Deployable Fin Systems for Missiles," AGARD Flight Vehicle Integration Conf., Ankara, Turkey, Oct. 1995.

[3] Abate, G. L., Swenson, M. N., and Whyte, R. H., "Aerodynamic Test and Analysis of Wrap-Around Fins at Supersonic Mach Numbers Utilizing Design of Experiments," AIAA Paper 94-0200, Jan. 1994.

[4] Dahlke, C. W., "The Aerodynamic Characteristics of Wrap-Around Fins at Mach Numbers of 0.3 to 3.0," U.S. Army Missile Command, TR RD-77-4, Redstone Arsenal, AL, Oct. 1976.

[5] Abate, G., "Aerodynamic Research of Wrap Around Fin Missile Configurations and Alternate Wrap Around Fin Designs," U.S. Air Force Wright Lab., WL-TR-94-7015, Eglin AFB, FL, Feb. 1994.

[6] Tilmann, C. P., Huffman, R. E., Jr., Buter, T. A., and Bowersox, R. D. W., "Experimental Investigation of the Flow Structure Near a Single

Wraparound Fin," *Journal of Spacecraft and Rockets*, Vol. 34, No. 6, 1997, pp. 729–736.

[7]Tilmann, C., and Bowersox, R., "Characterization of the Flowfield Near a Wrap-Around Fin at Mach 4.9," AIAA Paper 98-0684, Jan. 1998.

[8]Morris, M. J., Donovan, J. F., Kegelman, J. T., Schwab, S. D., and Levy, R. L., "Aerodynamic Applications of Pressure-Sensitive Paint," AIAA Paper 92-0264, Jan. 1992.

[9]Morris, M. J., and Donovan, J. F., "Application of Pressure- and Temperature-Sensitive Paints to High-Speed Flows," AIAA Paper 94-2231, June 1994.

[10]Goss, L. P., Gruber, M. R., and Nejad, A. S., "Surface Pressure Measurements in Supersonic Transverse Injection Flowfields," AIAA Paper 97-3254, July 1997.

[11]Sellers, M. E., "A Comparison of an AEDC and a Russian Developed Pressure Sensitive Paint in the AEDC Propulsion Wind Tunnel 16T," AEDC-TR-95-18, Arnold Engineering Development Center, TN, Dec. 1995.

J. R. Maus
Associate Editor